

SECOND-ORDER TOTAL VARIATION AND PRIMAL-DUAL ALGORITHM FOR CT IMAGE RECONSTRUCTION

SHOUSHENG LUO, QIAN LV, HESHAN CHEN, JINPING SONG

Abstract. In this paper, we proposed a regularization model based on second-order total variation for CT image reconstruction, which could eliminate the ‘staircase’ caused by total variation (TV) minimization. Moreover, some properties of second-order total variation were investigated, and a primal-dual algorithm for the proposed model was presented. Some numerical experiments for various projection data were conducted to demonstrate the efficiency of the proposed model and algorithm.

Key words. CT image reconstruction, regularization method, second-order total variation, primal-dual algorithm.

1. Introduction

Computed tomography (CT) is a noninvasive imaging technique, which plays an important role in modern medicine and industrial detections. CT image reconstruction methods have significant influence on the qualities of reconstructed images. These methods are mainly divided into two classes: analytical methods and algebraic methods [20, 27]. Generally speaking, the analytical methods, filtered back-projection for instance, are sensitive to noise, depend on the scan geometry and fail to deal with incomplete projection data. The algebraic methods, Kaczmarz method for example, are flexible for scan geometry and can deal with incomplete data partially, but suffer from high computation cost. However, algebraic methods attract increasingly attentions with the rapid development of computer technology. In this paper, we focus on the algebraic methods.

Approximating the unknown image by a 2D digital image $u \in \mathbb{R}^{m \times n}$ and denoting the intersection length of the i -th X-ray with the j -th pixel by a_{ij} (≥ 0), we can write the CT image reconstruction problem as to solve the following linear system [16, 20]

$$(1) \quad g = Au + \eta,$$

where $A = (a_{ij})_{M \times N}$ is called the imaging matrix, g is the projection data polluted by noise η , and u is the vector version of 2D image by lexicographic order. It is well known that recovering u from g by conventional direct methods is unfeasible due to the ill-posedness and large scale of A . Furthermore, neither analytical nor algebraic methods can handle incomplete (e.g. interior-CT) and heavily noised projection data.

Regularization techniques are important to reconstruct high quality image from incomplete and noised projection data. They are generally to minimize the following

Received by the editors November 25, 2015 and, in revised form, February 02, 2016.

2000 *Mathematics Subject Classification.* 92C55, 15A29.

This research was supported by National Natural Science Foundation of China (11471101, 11401117), Foundation of Henan Educational Committee of China (14B110019), Science and Technology Planning Project of Henan Province of China (132300410150).

energy function [21, 30, 32, 33]

$$(2) \quad u^* = \arg \min_u \{F(u) + \lambda G(u)\},$$

where F is called fidelity term measuring how fit Au is to the observation data g , and G is a convex function called regularization term representing prior knowledge. $\lambda (> 0)$ is an user-defined parameter to balance the two terms.

We need to select proper regularization and fidelity terms for practical problems on hand. For CT image reconstruction problem (1), the fidelity term is usually chosen as l^2 distance since the noise η obeys Gaussian distribution [20]. For the regularization term, there are many selections, such as total variation (TV) method [31, 33, 34] and l^1 regularization based on wavelet or tight-frame technique [41, 42]. Although the dictionary learning based approaches were studied in the literature [24, 39] recently, they are not popular in the field of CT image reconstruction because of their time consuming training step and the requirement for high efficiency in the CT image reconstruction field, and TV methods are still the most widely used methods because of its edge-preserving properties and simplicity.

However, TV model often causes staircase effects (i.e. false edges) in smooth regions [3, 6]. The staircases are caused by the fact that the TV minimization forces the smooth regions (nonconstant) to be piecewise constant. Therefore, although the performances of TV model are amazing for numerical simulations on piecewise constant phantoms in the literature, it is not yet applied to clinical and related practice so far since few real CT images are piecewise constant [30].

In order to overcome the spurious staircases of TV, higher-order total variations (typically, second-order total variation) have been of particular interest and studied thoroughly over the past two decades [2, 9, 10, 25]. High-order TV (HOTV) was used to prove the uniqueness of interior-CT reconstruction if the region of interest (ROI) is piecewise polynomial [40]. However, the numerical computation of HOTV used in [40] is difficult. Therefore, we try applying second-order total variation (called SOTV for short) to CT image reconstruction.

The SOTV was first proposed in [25] to remove additive noise. It has been studied mainly to suppress the staircase effects of TV. The theoretical analyses in [17, 36] show that SOTV is superior to TV in some aspects. The SOTV evolves an observed image toward a ‘smooth’ one theoretically. The reconstructions of SOTV are believed to be better than those of TV in smooth region. This property had been verified by numerical experiments [10, 25] as well. In addition, SOTV can be numerical implementation more easily than HOTV [40]. As far as we know, although SOTV was studied thoroughly in the field of image restoration, it was rarely used in image reconstruction. In view of the discussions above, we propose to use the SOTV as the regularization term of (2), and our numerical experiments show that our model can suppress the ‘staircase’ effects in smooth regions effectively.

It is well known that fast and stable algorithm is crucial for the application of regularization model (2). Because of the non-smoothness of SOTV, a lot of algorithms (for example Newton method) are unfeasible. Recently, some algorithms have been proposed to tackle the non-smooth optimal problem, such as split Bregman iteration method [11, 15], primal-dual (PD) algorithm [5, 7, 43], alternative direction method of multiplier [29] and fixed-point algorithm [23, 26]. The PD algorithm, which was first proposed in [1], was investigated thoroughly [12, 18] and applied to solve the large scale problem in imaging science recently, such as image reconstruction [28, 38], restoration [37] and segmentation [8]. The PD algorithm is a general frame which can cover many models in image processing. In this paper,

we chose the PD algorithm [7] to solve the proposed model and deduce the precise implementation formulae. For a primal problem

$$(3) \quad \min_x \{F(Kx) + G(x)\},$$

where $x \in \mathbb{R}^N$, K is a linear operator, G and F are convex functions, the frame of PD algorithm can be illustrated as algorithm 1 (see [7, 32] for details).

Algorithm 1 Pseudocode of PD algorithm

- 1: Initialization: Choose $\tau, \sigma > 0$ such that $\tau\sigma\|K\|_2^2 \leq 1$, $\theta \in [0, 1]$, $x_0 = 0$, $y_0 = 0$, $\bar{x}_0 = x_0$, $n = 0$;
- 2: Iterations ($n \geq 1$): Update x_n , y_n , \bar{x}_n as follows

$$\begin{cases} y_{n+1} = \text{prox}_\sigma[F^*](y_n + \sigma K\bar{x}_n), \\ x_{n+1} = \text{prox}_\tau[G](x_n - \tau K^T y_{n+1}), \\ \bar{x}_{n+1} = x_{n+1} + \theta(x_{n+1} - x_n). \end{cases}$$

In algorithm 1, $\|K\|_2$ is the norm of operator K . The superscript ‘*’ and prox_σ refer to convex conjugation and the proximal mapping of any convex function. Let H be a convex function, then

$$(4) \quad H^*(z) = \max_{z'} \{\langle z, z' \rangle - H(z')\},$$

$$(5) \quad \text{prox}_\sigma[H](z) = \arg \min_{z'} \{H(z') + \frac{\|z - z'\|_2^2}{2\sigma}\}.$$

In order to apply the PD algorithm to the proposed model, we should investigate the conjugate function of second-order total variation and the corresponding proximal mapping (see details in Section 2.2).

The rest of this paper is organized as follows. In section 2, we present the SOTV model, its properties and the corresponding PD algorithm. Numerical experiments for various projection data in section 3 are presented to compare SOTV model with TV model and adaptive framelet tensor method (ATF) proposed in [42]. Some conclusions and comments are given in section 4.

2. The Proposed Model and Primal-Dual Algorithm

We introduce some notations for convenience. Denote

$$(6) \quad Y = \left\{ p \mid p = \begin{pmatrix} p^{11} & p^{12} \\ p^{21} & p^{22} \end{pmatrix}, p^{kl} \in \mathbb{R}^{m \times n}, k, l = 1, 2 \right\}.$$

For $p = \begin{pmatrix} p^{11} & p^{12} \\ p^{21} & p^{22} \end{pmatrix}$, $q = \begin{pmatrix} q^{11} & q^{12} \\ q^{21} & q^{22} \end{pmatrix} \in Y$, the inner-product is introduced as

$$(7) \quad \langle p, q \rangle_Y = \sum_{i=1}^m \sum_{j=1}^n (p_{ij}^{11} q_{ij}^{11} + p_{ij}^{12} q_{ij}^{12} + p_{ij}^{21} q_{ij}^{21} + p_{ij}^{22} q_{ij}^{22}).$$

For $u \in X = \mathbb{R}^{m \times n}$ or $u \in \mathbb{R}^N$ ($N = mn$) in the context, the discrete Hessian matrix of u is defined as

$$(8) \quad \nabla^2 u = \begin{pmatrix} \nabla_x^-(\nabla_x^+ u) & \nabla_y^+(\nabla_x^+ u) \\ \nabla_x^-(\nabla_y^- u) & \nabla_y^-(\nabla_y^+ u) \end{pmatrix} \in Y,$$

where $(\nabla_x^\pm u)_{ij} = \pm(u_{(i\pm 1)j} - u_{ij})$, $(\nabla_y^\pm u)_{ij} = \pm(u_{i(j\pm 1)} - u_{ij})$ with boundary conditions $u_{0j} = u_{(1+m)j} = u_{i0} = u_{i(1+n)} = 0$ for any $i = 1, 2, \dots, m$, $j = 1, 2, \dots, n$. The second-order TV of an image $u \in X = \mathbb{R}^{m \times n}$ is defined as [10]

$$\|(|\nabla^2 u|)\|_1 = \sum_{i=1}^m \sum_{j=1}^n |\nabla^2 u_{ij}|,$$

where

$$|\nabla^2 u_{ij}| = \sqrt{(\nabla_x^-(\nabla_x^+ u))_{ij}^2 + (\nabla_y^+(\nabla_x^+ u))_{ij}^2 + (\nabla_x^-(\nabla_y^- u))_{ij}^2 + (\nabla_y^-(\nabla_y^+ u))_{ij}^2}.$$

2.1. The Proposed Model and the Existence of Solutions. For an image $u \in X = \mathbb{R}^{m \times n}$ or $u \in \mathbb{R}^N$ ($N = mn$), the proposed SOTV-based CT image reconstruction model is

$$(9) \quad \min_{u \in \mathbb{R}_+^N} \left\{ \frac{1}{2} \|Au - g\|_2^2 + \lambda \|(|\nabla^2 u|)\|_1 \right\},$$

where $\mathbb{R}_+^N = \{u : u \in \mathbb{R}^N \text{ and } u \geq 0\}$ with $u \geq 0$ meaning that all the components of u are nonnegative. Here the nonnegative constraint $u \in \mathbb{R}_+^N$ is needed since the image u is nonnegative in practice.

Lemma 1. Let $W_1(u) = \|Au - g\|_2^2$, where $A = (a_{ij})_{M \times N}$ with $a_{ij} \geq 0$ ($i = 1, \dots, M, j = 1, \dots, N$) and $\sum_{i=1}^M a_{ij} > 0$ ($\forall j$), then W_1 is coercive.

Proof: Firstly, by the triangle inequality

$$(10) \quad \|Au - g\|_2 \geq \|Au\|_2 - \|g\|_2.$$

Furthermore, we have

$$(11) \quad \|Au\|_2^2 = \sum_{i=1}^M \left(\sum_{j=1}^N a_{ij} u_j \right)^2 \geq \sum_{i=1}^M \sum_{j=1}^N (a_{ij} u_j)^2 = \sum_{j=1}^N \left(\sum_{i=1}^M a_{ij}^2 \right) u_j^2,$$

where the inequality held by $a_{ij} \geq 0$ and $u \in \mathbb{R}_+^N$. Therefore, when $\|u\|_2 \rightarrow \infty$, i.e. there is at least one index $t \in \{1, 2, \dots, N\}$ such that $u_t \rightarrow +\infty$, we can get $\left(\sum_{i=1}^M a_{it}^2 \right) u_t^2 \rightarrow +\infty$ by the assumption $\sum_{i=1}^M a_{it} > 0$. By (10) and (11), we can obtain the conclusion.

Theorem 1. Under the assumptions of Lemma 1 and $\lambda > 0$, the solution set of (9) is nonempty.

Proof: Let

$$W(u) = \frac{1}{2} \|Au - g\|_2^2 + \lambda \|(|\nabla^2 u|)\|_1,$$

clearly, W is the objective function of the proposed model (9). The nonnegative set \mathbb{R}_+^N is a closed and convex subset of Hilbert space \mathbb{R}^N . Therefore, it is sufficient for the conclusion to prove that W is a weakly lower semicontinuous and coercive function on \mathbb{R}_+^N by Theorem 2.30 in [35]. Obviously, W is convex and hence weakly lower semicontinuous on \mathbb{R}_+^N . By Lemma 1 and the nonnegativity of the second term of W , the coerciveness of W is proved. Therefore, the solution to (9) is nonempty.

Remark 1. In fact, the CT imaging matrix A in (1) satisfies the conditions in Lemma 1. Firstly, $a_{ij} \geq 0$ ($i = 1, \dots, M, j = 1, \dots, N$) since it denotes the intersection length of i -th X-ray with j -th pixel. Secondly, for any pixel, it is reasonable to assume that there is at least one X-ray intersects with it (otherwise

this pixel is not in the field of view, thus it's impossible to reconstruct it), hence all column sums of A are positive, i.e. $\sum_{i=1}^M a_{ij} > 0$ ($\forall j$).

Remark 2. If W_1 is a strictly convex function, for example A is a column full rank matrix, i.e. $\text{Null}(A)=\{0\}$, the minimization problem (9) has an unique solution.

2.2. The Primal-Dual Algorithm for the Proposed Model. In order to deduce the PD algorithm for the proposed model (9) (called PD-SOTV for short), we introduce the following notations

$$(12) \quad F(y, z) = F_1(y) + F_2(z),$$

$$(13) \quad G(u) = \delta_+(u) = \begin{cases} 0 & u \geq 0 \\ +\infty & \text{otherwise} \end{cases},$$

$$(14) \quad K = \begin{pmatrix} A \\ \nabla^2 \end{pmatrix},$$

with $F_1(y) = \frac{1}{2}\|y - g\|_2^2$, $F_2(z) = \lambda\|(|z|)\|_1$. Therefore, the proposed model (9) can be rewritten as

$$(15) \quad \min_u \{F(Ku) + G(u)\},$$

with $y = Au$, $z = \nabla^2 u$.

Proposition 1. (reference [32]) By definitions (4) and (5), we have

$$(16) \quad F_1^*(p) = \frac{1}{2}\|p\|_2^2 + \langle p, g \rangle,$$

the proximal mapping of F_1^* and G are

$$(17) \quad \text{prox}_\sigma[F_1^*](y) = \frac{y - \sigma g}{1 + \sigma},$$

$$(18) \quad \text{prox}_\tau[G](u) = \arg \min_y \left\{ \delta_+(y) + \frac{\|u - y\|_2^2}{2\tau} \right\} = \max\{0, u\}.$$

Proposition 2. (1) The convex conjugation of F_2 is

$$(19) \quad F_2^*(q) = \delta_{\text{Box}(\lambda)}(|q|),$$

where $\delta_{\text{Box}(\lambda)}(u) = \begin{cases} 0 & \|u\|_\infty \leq \lambda \\ \infty & \text{otherwise} \end{cases}$, and $\text{Box}(\lambda)$ consists of vectors with no component larger than λ .

(2) The proximal mapping of F_2^* is

$$(20) \quad \text{prox}_\sigma[F_2^*](z) = \frac{\lambda z}{\max(\lambda \mathbf{1}_I, |z|)},$$

where the division means componentwise division.

Proof: (1) By the definition (4), we have

$$(21) \quad F_2^*(q) = \max_z \{ \langle q, z \rangle_Y - \lambda \|(|z|)\|_1 \},$$

Let $h(z) = \langle q, z \rangle_Y - \lambda \|(|z|)\|_1$. Then we have

$$(22) \quad \begin{aligned} h(z) &\leq \sum_{i=1}^m \sum_{j=1}^n |q_{ij}| |z_{ij}| - \lambda \sum_{i=1}^m \sum_{j=1}^n |z_{ij}| \\ &= \sum_{i=1}^m \sum_{j=1}^n (|q_{ij}| - \lambda) |z_{ij}|, \end{aligned}$$

by Cauchy-Schwarz inequality, where the equality holds if and only if $z_{ij} = t_{ij}q_{ij}$ ($t_{ij} \geq 0, \forall i, j$). There are two cases to be considered. (A) $|q| \in \text{Box}(\lambda)$, i.e. $|q_{ij}| \leq \lambda$ ($\forall i, j$). In this case, it is obvious that $h(z) \leq 0$. (B) $|q| \notin \text{Box}(\lambda)$, i.e. there is at least one pixel of $|q|$ greater than λ . Let us assume $|q_{kl}| > \lambda$ ($k \in \{1, \dots, m\}, l \in \{1, \dots, n\}$). Obviously, if $t_{ij} = 0$ ($i \neq k, j \neq l$) and $t_{kl} \rightarrow +\infty$, then $h(z) \rightarrow +\infty$ also. Putting these two cases together, we have formula (19).

(2) By the definition (5), we have

$$(23) \quad \text{prox}_{\sigma[F_2^*]}(z) = \arg \min_{z'} \left\{ \delta_{\text{Box}(\lambda)}(|z'|) + \frac{\|z - z'\|_Y^2}{2\sigma} \right\}$$

$$(24) \quad = \frac{\lambda z}{\max\{\lambda, |z|\}}$$

since $|z'_{ij}| \leq \lambda, \forall i = 1, \dots, m, j = 1, \dots, n$. Thus we get formula (20).

Combining formula (17), (18) and (20), we get the following PD-SOTV algorithm (algorithm 2) for the proposed SOTV model (9).

Algorithm 2 The PD-SOTV algorithm

- 1: $L \geq \|(A, \nabla^2)\|_2; \tau = 1/L; \sigma = 1/L;$
 - 2: initialize u_0, p_0 and q_0 to zero values, $\bar{u}_0 = u_0;$
 - 3: **for** $n = 1$ to N **do**
 - 4: $p_{n+1} = p_n + \sigma(A\bar{u}_n - g)/(1 + \sigma)$
 - 5: $q_{n+1} = \lambda(q_n + \sigma\nabla^2\bar{u}_n)/\max(\lambda\mathbf{1}_I, |q_n + \sigma\nabla^2\bar{u}_n|)$
 - 6: $u_{n+1} = \max\{0, u_n - \tau A^T p_{n+1} - \tau \text{div}^2(q_{n+1})\}$
 - 7: $\bar{u}_{n+1} = u_{n+1} + \theta(u_{n+1} - u_n)$
 - 8: **end for**
-

where div^2 denotes the conjugate operator of ∇^2 [10].

3. Numerical Experiments

In this section, some numerical experiments are presented to test the proposed model and algorithm. For all the experiments, the phantoms are digitalized on a grid of 200×200 and the original projection data are corrupted by zero mean Gaussian noise ($G(0, \sigma^2)$). Hereafter, the data is called ‘complete’ when they are generated at views ranging from 0° to 180° evenly and each projection containing 200 evenly spaced parallel rays. Otherwise, the projection data is ‘incomplete’. In the simulations, the imaging matrix A in (1) is computed row by row by using a simple geometry relationship (see [19] for details).

We will compare the reconstruction results of SOTV with those of TV and ATF method [42] for a modified 2D Shepp-Logan phantom [40] with complete and incomplete data (interior-CT), respectively. In addition, experiments on a ghost phantom [13, 21] with incomplete project data are presented to illustrate the efficiency of the proposed model for more challenging image reconstruction problems. For ATF method [42], we chose B-spline as the initial framelet to construct the adaptive tensor framelet and also used PD algorithm to solve the reconstruction problem. The parameter λ in the algorithm is optimized by trial and error.

3.1. Modified Shepp-Logan Phantom with Complete Data. The modified 2D Shepp-Logan phantom shown in top left in Figure 1 is the combination of four linear functions and six constant functions in the ellipses with the parameters listed in table 1. In each ellipse, the function was first defined inside a compact support

TABLE 1. Parameters of the 2D modified Shepp-Logan phantom.

k	a_k	b_k	μ_k	r_k	x_k^0	y_k^0	α_k
1	0.92	0.69	1	0	0	0	90
2	0.874	0.6624	-0.8	0	0	-0.0184	90
3	0.35	0.15	-0.1	1	0.25	-0.05	72
4	0.45	0.2	-0.1	1	-0.28	-0.05	108
5	0.35	0.3	0.1	1	0	0.43	90
6	0.046	0.046	0.1	1	0	0.1	0
7	0.046	0.046	0.1	1	0	-0.1	0
8	0.046	0.023	0.1	1	-0.08	-0.605	0
9	0.023	0.023	0.1	1	0	-0.605	0
10	0.046	0.023	0.1	1	0.06	-0.605	90

$\Omega_k = \{(x, y) \in \mathbb{R}^2 : \frac{x^2}{a_k^2} + \frac{y^2}{b_k^2} < 1\} (k = 1, 2, \dots, 10)$ as $(\frac{y \cdot r_k}{b_k} + 1)\mu_k$, and then its center was translated to (x_k^0, y_k^0) and rotated by an angle α_k (see [40]). Two small parts of original phantom shown in middle row and bottom row of Figure 1 are emphasized to compare the performances of different models on different regions, respectively.

A lot of numerical experiments were conducted for different projection data corrupted by Gaussian noise with variance ranging from 0.001 to 0.02. From Figure 1, we observed that both TV and ATF methods cause ‘staircase’ effect and this effect became more obvious as the noise got more heavy, and the performances of the proposed model were better than those of TV and ATF when the variance ranged from 0.003 to 0.02, especially for piecewise smooth (linear) regions. Due to the space limitations, we only presented the reconstruction results in Figure 1 by different methods with $\sigma^2 = 0.005$.

Comparing the images in the middle row of Figure 1, we can clearly observe that TV and ATF both cause strong ‘staircase’ effect, while SOTV suppresses ‘staircase’ efficiently. However, we can also see that TV and ATF preserved while SOTV blurred edges and details by comparing the images in the last row of Figure 1. This is because the TV method and the framelet method have some connections (see [4] for details).

In order to evaluate different methods quantitatively, the MSEs (mean square errors) of two regions of interest in Figure 1 were computed and presented in Table 2. We can obtain the same conclusion that the proposed model is better than TV and ATF in piecewise linear regions, and TV and ATF are superior to SOTV in piecewise constant regions.

TABLE 2. MSEs for two parts of the images in Figure 1.

	TV	SOTV	ATF
Part 1	0.0046	0.0029	0.0039
Part 2	0.0220	0.0672	0.0241

The profiles of the 90th vertical line of different reconstruction images were plotted in Figure 2 to illustrate the properties of different methods further. In order to differentiate these profiles easily, a small value 0.02 was added to SOTV profile, and subtracted 0.02 and 0.04 from TV and ATF, respectively. Then we can clearly see that the profiles of TV and ATF models look like ‘staircase’ in the linear part, while profile of SOTV can suppress it successfully.

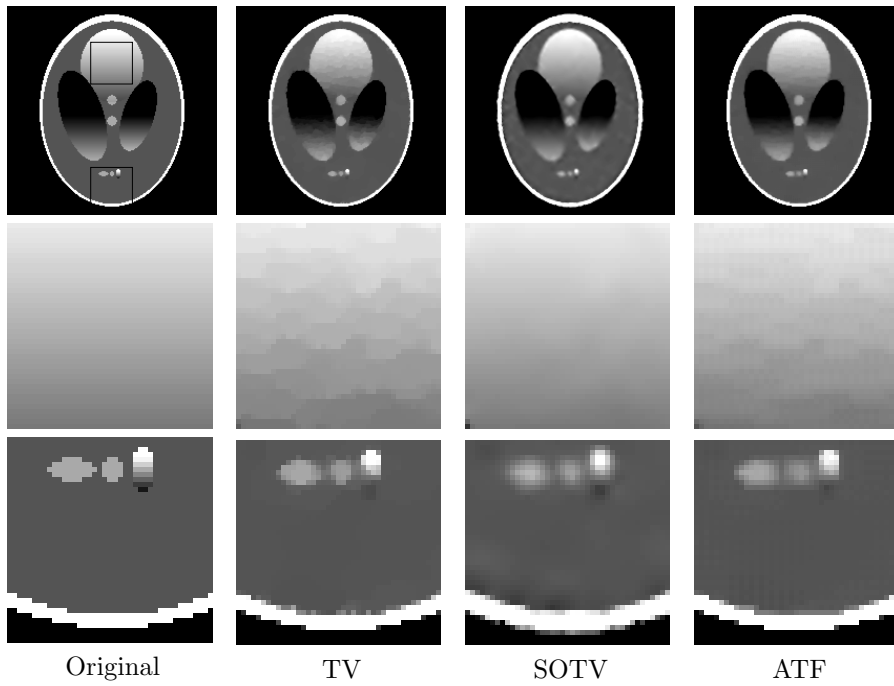


FIGURE 1. Top row: Reconstructions with complete data. Middle row: Reconstructions of Part 1. Bottom row: Reconstructions of Part 2.

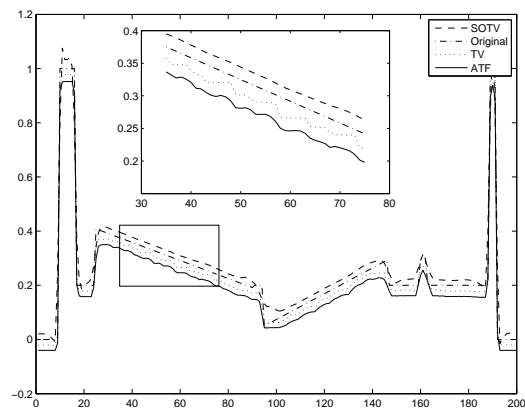


FIGURE 2. The 90th vertical lines of the images in Figure 1.

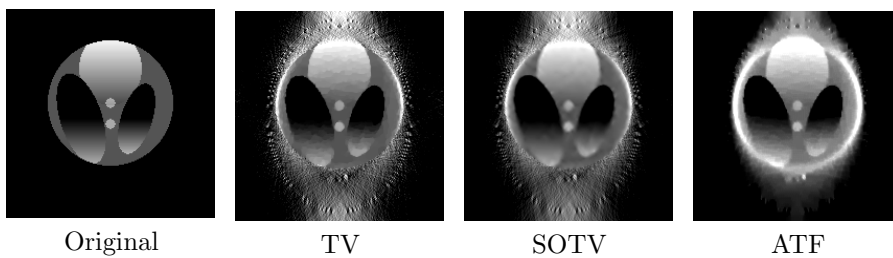


FIGURE 3. Reconstructions of ROI.

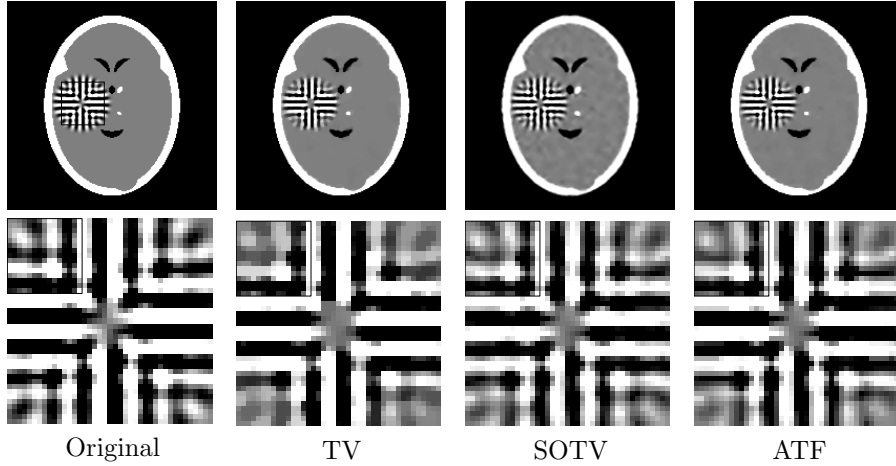


FIGURE 4. Top row: Reconstructions from 142 projections. Bottom row: Zoom in of ghost part.

3.2. Interior-CT of Modified Shepp-Logan. Region of interest (ROI) image reconstruction for CT has received more and more attentions recently since it can reduce the dose of radiation and acquaintance time [14, 22, 40]. The interior-CT, which only radiates to a small region of interest, is one of the important ROI problems. Interior-CT tends to be severely ill-posed, and reconstructions by directly algorithms, such as FBP and ART, usually suffer from serious artifacts [27]. Regularization reconstruction is one of the possible techniques to handle interior-CT problems [40].

In the simulations, the projection data only consisted of the X-ray which pass through the disk with center $(0,0.1)$ and radius 0.6 (denoted by Disk $(0,0.1,0.6)$). The reconstructed images by SOTV, TV and ATF were presented in Figure 3. From Figure 3, we can observe that all three methods can reconstruction ROI approximately, but TV and ATF still suffer from ‘staircase’ effect. The MSEs of the reconstructed ROI by SOTV, TV and ATF methods were 0.1253 , 0.1306 and 0.1250 , which showed the proposed model was better than TV and ATF because this ROI is piecewise linear. In addition, we can observe that the result by ATF method suffers from wider blurring edge.

3.3. Ghost Phantom with 142 Projection Views. In order to evaluate the proposed model further, we applied the proposed model to a more challenging phantom (Figure 4), which contains a ghost function that is invisible from given 22 projection directions (see [21] for details). The existence of ghosts has been known and studied since the earliest days of CT, see section 16.4 of [19]. Here, the projection data was generated at 142 angles, which contained 120 angles ranging from 0° to 180° evenly and the 22 given projection directions.

From Figure 4, we can clearly see TV causes ‘staircase’ in ghost, especially in the center and corners, while SOTV and ATF get better results. Moreover, Figure 5 shows that SOTV and ATF can preserve more details of ghost part than TV model. In addition, the MSE of ghost part of SOTV model (0.0481) and ATF (0.0428) both are smaller than that of TV model (0.0564). All these results demonstrate the efficiency of our model in preserving details and supressing staircase of TV.

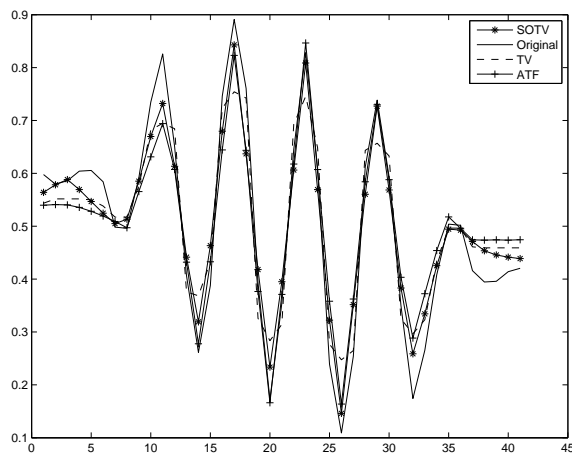


FIGURE 5. Profiles of the 9th vertical line of the images in the second row of Figure 4.

4. Conclusions and Future Works

The studies about reconstruction model are fewer than the algorithm studies in the literature. In this paper, we proposed a regularization model based on SOTV for CT image reconstruction, which was an attempt to promote the development of regularization model. Numerical experiments showed that the proposed model, the TV and ATF models had merits and demerits. The proposed model can suppress the ‘staircase’ effects in smooth regions caused by TV and ATF. However, TV and ATF are superior to the SOTV model in piecewise constant regions and allow for discontinuities (see Figure 1 and Figure 3). Therefore, it is our future work to study the combination of them, which maintains their merits and avoids their demerits at the same time. Since all the experiments in this paper were carried out on the simulated projection data, we need to verify the proposed model on practical data in the future.

Acknowledgments

The author thanks the anonymous authors whose work largely constitutes this sample file. This research was supported by National Natural Science Foundation of China (11471101, 1140117), Foundation of Henan Educational Committee of China (14B110019), Science and Technology Planning Project of Henan Province of China (132300410150). The authors wish to thank Professor Xiaobing Feng (University of Tennessee, Knoxville), Professor Xuecheng Tai (University of Bergen, Norway), Professor Tie Zhou (Peking University) and Professor Zhifeng Pang (Henan University) for helpful discussions and comments.

References

- [1] K. Arrow, L. Hurwicz and H. Uzawa, *Studies in Linear and Non-linear Programming*. Stanford Mathematical Studies in the Social Sciences. Stanford University Press, California, 1958.
- [2] K. Bredies, K. Kunisch and T. Pock, Total generalized variation, *SIAM Journal on Image Sciences*, 3 (2010) 492-526.
- [3] A. Buades, B. Coll and J. M. Morel, The staircasing effect in neighborhood filters and its solution, *IEEE Trans. Image Process.*, 15 (2006) 1499-1505.
- [4] J. Cai, B. Dong, S. Osher and Z. Shen, Image restoration: total variation, wavelet frames, and beyond, *Journal of the American Mathematical Society*, 25 (4) (2012), 1033-1089.

- [5] A. Chambolle, An algorithm for total variation minimization and applications, *J. Math. Imaging Vision*, 20 (2004) 89-97.
- [6] A. Chambolle and P. L. Lions, Image recovery via total variation minimization and related problems, *Numer. Math.*, 76 (1997) 167-188.
- [7] A. Chambolle and T. Pock, A first-order primal-dual algorithm for convex problem with applications to imaging, *J. Math. Imaging Vision*, 40 (2011) 120-145.
- [8] R. Chan, H. Yang and T. Zeng, A Two-Stage Image Segmentation Method for Blurry Images with Poisson or Multiplicative Gamma Noise, *J. Imaging Sci*, 7 (2014) 98-127.
- [9] T. Chan, S. Esedoglu and F. E. Park, *A fourth order dual method for staircase reduction in texture extraction and image restoration problems*. In Proceedings of IEEE International Conference on Image Processing, p. 4137-4140, Hong Kong, 2005.
- [10] H. Chen, J. Song and X. Tai, A dual algorithm for minimization of the LLT model, *Adv. Comput. Math.*, 31 (2009) 115-130.
- [11] Y. Chen, W. Hager, M. Yashtini, X. Ye and H. Zhang, Bregman operator splitting with variable stepsize for total variation image reconstruction, *Comput. Optim. Appl.*, 54 (2013) 317-342.
- [12] Y. Chen, G. Lan and Y. Ouyang, Optimal primal-dual methods for a class of saddle point problems, *SIAM J. Optim.*, 24 (2013) 1779-1814.
- [13] R. Davidi, G. T. Herman and J. Klukowska, SNARK09: A programming system for the reconstruction of 2D images from 1D projections, <http://www.dig.cs.gc.cuny.edu/software/snark09/SNARK09.pdf>, 2014.
- [14] A. Faridani, E. L. Ritman and K. T. Smith, Local tomography, *SIAM J. Appl. Math.*, 52 (1992) 459-484.
- [15] T. Goldstein and S. Osher., The split bregman algorithm for L^1 regularized problems, *SIAM J. Imaging Sci*, 2 (2009) 323-343.
- [16] R. Gordon, R. Bender and G. T. Herman, Algebraic reconstruction techniques (ART) for three-dimensional electron microscopy and X-ray photography, *J. Theor. Biol.*, 29 (1970) 471-481.
- [17] J. B. Greer and A. L. Bertozzi, H^1 solutions of a class of fourth order nonlinear equations for image processing, *Discrete Contin. Dyn. Syst.*, 1-2 (2004) 349-366.
- [18] B. He and X. Yuan, Convergence analysis of primal-dual algorithms for a saddlepoint problem: From contraction perspective, *SIAM J. Imaging Sci.*, 5 (2012) 119-149.
- [19] G. T. Herman, *Image Reconstruction from Projections: The Fundamentals of Computerized Tomography*, Academic Press, New York, 1980.
- [20] G. T. Herman, *Fundamentals of Computerized Tomography: Image Reconstruction from Projections*, Springer, 2nd edition, 2009.
- [21] G. T. Herman and R. Davidi, Image reconstruction from a small number of projections, *Inverse Problems*, 24 (2008) 045011.
- [22] H. Kudo, M. Courdurier, F. Noo and M. Defrise, Tiny a priori knowledge solves the interior problem in computed tomography, *Phys. Med. Biol.*, 53 (2008) 2207-2231.
- [23] Q. Li, C. A. Micchelli, L. Shen and Y. Xu, A proximity algorithm accelerated by Gauss-Seidel iterations for L1/TV denoising models, *Inverse Problems*, 28 (2012) 095003.
- [24] S. Li, Q. Cao, Y. Chen, Y. Hu, L. Luo and C. Toumoulin, Dictionary learning based sinogram inpainting for CT sparsereconstruction, *Optik*, 125 (2014) 2862-2867.
- [25] M. Lysaker, A. Lundervold and X. Tai, Noise removal using fourthorder partial differential equation with applications to medical magnetic resonance images in space and time, *IEEE Trans. Image Process.*, 12 (2003) 1579-1590.
- [26] C. A. Micchelli, L. Shen and Y. Xu, Proximity algorithms for image models: denoising, *Inverse Problems*, 27 (2011) 045009.
- [27] F. Natterer, *The Mathematics of Computerized Tomography*, Philadelphia, 1986.
- [28] J. Niesen and A. Sawatzky, Performance of primal-dual algorithms for multi-channel image reconstruction in spectral X-Ray CT, *Proc. IEEE Nucl. Sci. Symp. Med. Imaging Conf.*, (2014).
- [29] Y. Ouyang, Y. Chen and G. Lan, An accelerated linearized alternating direction method of multipliers, *SIAM J. Imaging Sci.*, 8 (2015) 644-681.
- [30] X. Pan, E. Y. Sidky and M. Vannier, Why do commercial CT scanners still employ traditional, filtered backprojection for image reconstruction? *Inverse Problems*, 25 (2009) 123009.
- [31] L. I. Rudin, S. Osher and E. Fatemi, Nonlinear total variation based noise removal algorithms, *Physica D*, 60 (1992) 259-268.

- [32] E. Y. Sidky, J. H. Jorgensen and X. Pan, Convex optimization problem prototyping for image reconstruction in computed tomography with the Chambolle-Pock algorithm, *Phys. Med. Biol.*, 57 (2012) 3065-3091.
- [33] E. Y. Sidky, C. M. Kao and X. Pan, Accurate image reconstruction from fewviews and limited-angle data in divergent-beam CT, *J. X-ray Sci. Technol.*, 14 (2006) 119-139.
- [34] D. Strong and T. Chan, Edge-preserving and scale-dependent properties of total variation regularization, *Inverse Problems*, 19 (2003) 165-187.
- [35] C. R. Vogel, *Computational Methods for Inverse Problems*, SIAM, Philadelphia, 2002.
- [36] J. Weickert, *Anisotropic Diffusion in Image Processing*, B.G. Teubner, Stuttgart, 1998.
- [37] Y. Wen, R. H. Chan and T. Zeng, Primal-dual algorithms for total variation based image restoration under Poisson noise, *SCI China Math*, 59 (2016) 141-160.
- [38] P. Wolf, J. H. Jorgensen, T. Schmidt, E. Y. Sidky, A first-order primal-dual reconstruction algorithm for few-View SPECT, *Proc. IEEE Nucl. Sci. Symp. Med. Imaging Conf.*, (2012) 2381-2385.
- [39] Q. Xu, H. Yu, X. Mou, L. Zhang, J. Hsieh and G. Wang, Low-dose X-ray CT reconstruction via dictionary learning, *T. Med. Imaging*, 31 (2012) 1682-1697.
- [40] J. Yang, H. Yu, M. Jiang and G. Wang, High-order total variation minimization for interior tomography, *Inverse Problems*, 26 (2010) 035013.
- [41] B. Zhao, H. Gao, H. Ding and S. Molloi, Tight-frame based iterative image reconstruction for spectral breast CT, *Med. Phys.*, 40 (2013) 031905.
- [42] W. Zhou, J. Cai and H. Gao, Adaptive tight frame based medical image reconstruction: a proof-of-concept study for computed tomography, *Inverse Problems*, 29 (2013) 125006.
- [43] M. Zhu and T. Chan, An efficient primal-dual hybrid gradient algorithm for total variation image restoration, *UCLA CAM Report*, 34 (2008).

School of Mathematics and Statistics, Henan University, Kaifeng, Henan, 475001, China
E-mail: Luo.ssheng@163.com and 1601110034@pku.edu.cn and heshanchen@henu.edu.cn and songjp@henu.edu.cn